Batteries & Supercaps

Research Article
doi.org/10.1002/batt.202400426

Chemistry
Europe
European Chemical
Societies Publishing

www.batteries-supercaps.org

Ethanediamine Intercalation Induced Hydrogen Bond Network in Vanadium Oxide for Ultralong-Life Aqueous Ammonium Ion Batteries

Tzu-Hao Lu,[a, b] Qiyu Liu,[b] Jinjun He,[b] Hao Liu,[b] Yanxia Yu,*[b] Yi Wang,*[a] and Xihong Lu*[b]

Aqueous ammonium-ion batteries (AAIBs) have received tremendous attention as a potential energy technology, but their development is severely challenged by the fact that the as-reported electrode materials are usually unable to meet the requirements of high capacity and high stability simultaneously. Herein, an organic-inorganic hybrid material of ethanediamine (EDA) intercalated vanadium oxide (VO-EDA) is synthesized as a high-performance anode material for AAIBs. The intercalated EDA molecules not only act as an electron donor to bind with NH$_4^+$, but also form hydrogen bonding network structures with vanadium oxides to facilitate charge/ion transfer. As a result, this hybrid material provides a high specific capacity of 104.4 mAh g^{-1} at 0.5 A g^{-1} and good cycling stability after 5000 cycles 10 A g^{-1} with a coulombic efficiency of ~100%. Moreover, the ammonium-ion full cell based on VO-EDA anode and NiHCF cathode achieves a specific capacity of 55 mAh g^{-1} at 0.1 A g^{-1} and impressive cycling stability with 88.6% capacity retention after 10000 cycles at 5 A g^{-1}.

Introduction

The rapid growth of renewable energy, such as photovoltaics and solar power, has created tremendous demands in scalable energy storage technologies to cope with the inherent intermittency of these energy sources. Although lithium-ion batteries (LIBs) dominate the battery market due to their high energy density and long cycle life, the further application of LIBs in large scale energy storage systems has been hindered by the potential safety hazards associated with organic electrolytes and scarcity of Li resources. Aqueous rechargeable batteries (ARBs), which feature reliable safety, low cost and environmental friendliness, have shown great potential for large-scale energy systems.[1,2] Up to now, ARBs involving metal ions (Al^{3+},[3] Zn^{2+},[4–6] Mg^{2+},[7] Ca^{2+},[8] Li$^+$,[9] Na$^+$,[10,11] K$^+$[12]) as charge carries have been extensively studied, but the large metal ion radii often result in lower diffusion kinetics. In contrast, ammonium ion (NH$_4^+$) has the smallest hydrated ionic size (3.3 Å), which can facilitate fast diffusion in aqueous electrolytes.[13] In addition, compared to other nonmetallic cations, e.g., proton (H$^+$) and hydronium (H$_3$O$^+$), NH$_4^+$ is weakly corrosive to electrode materials. Especially, NH$_4^+$ also exhibit some other characteristics, such as ultralow molar mass

(18 g mol^{-1}), unique hydrogen bond coordination structure and abundant reserves.[14] Therefore, aqueous ammonium ion batteries (AAIBs) have attracted much attention in recent years.

To date, a number of electrode materials have been explored for AAIBs, including Prussian blue analogues (KCu[Fe-(CN)$_6$], (NH$_4$)$_{1.47}$Ni[Fe(CN)$_6$]$_2$]$_{0.88}$, Fe[Fe(CN)$_6$]$_{0.88}$, NiHCF@CNTs),[15–18] Mn-based compounds (MnO$_x$, Mn$_3$(PO$_4$)$_2 \cdot$7H$_2$O),[19,20] V-based oxides (V$_2$O$_5 \cdot$H$_2$O, monoclinic VO$_2$, VOPO$_4 \cdot$H$_2$O)[21–23] and other metal oxides (h-MoO$_3$, WO$_3$).[24,25] In particular, vanadium-based materials own the significant attention due to cost economical (~US \$7.85/1b) and high theoretical capacity (589.0 mAh g^{-1} based on two-electron transport).[26] For instance, Ji and his co-worker reported a bi-layer hydrated V$_2$O$_5$ with capacity of 103 mAh g^{-1} for the· AAIBs.[21] Mai's group developed a polyaniline intercalated vanadium oxide for NH$_4^+$ storage. Although this electrode delivered high capacity of 138 mAh g^{-1}, it decreased by ~44% after 100 cycles.[27] Zhang et al reported a NH$_4$V$_4$O$_{10}$ electrode for NH$_4^+$ storage, which exhibits a capacity of 112.3 mAh g^{-1} and assembled the full cell with capacity of 58.5 mAh g^{-1}.[28] Despite the above-mentioned progresses, the reported electrode materials or ammonium ion full battery generally suffer from poor rate capability, inferior structural stability or insufficient capacity. Therefore, it is highly desirable to design a new type of materials for reversible NH$_4^+$ storage that have excellent electrochemical performance.

Herein, we fabricated an organic-inorganic hybrid material of ethanediamine (EDA) intercalated vanadium oxide (denoted as VO-EDA) using one-step solvothermal method for NH$_4^+$ storage. The polar group –NH$_2$ in EDA could bind to NH$_4^+$ as an electron donor, while the H-bond coordination structure between EDA and VO can promote the charge transport, thus effectively enhancing the capacity and stability of the host material. The as-prepared VO-EDA electrode displays a high specific capacity of 104.4 mAh g^{-1} at 0.5 A g^{-1}, much higher than the pristine VO–N (24.7 mAh g^{-1}). In addition, VO-EDA

[a] T.-H. Lu, Y. Wang
College of Chemistry and Material Engineering, Guiyang University,
Guiyang, Guizhou 550005, P. R. China
E-mail: wy742011@hotmail.com

[b] T.-H. Lu, Q. Liu, J. He, H. Liu, Y. Yu, X. Lu
The Key Lab of Low-carbon Chem & Energy Conservation of Guangdong
Province, School of Chemistry, School of Chemical Engineering and
Technology, Sun Yat-Sen University, Guangzhou 510275, P. R. China
E-mail: yuyx26@mail.sysu.edu.cn
luxh6@mail.sysu.edu.cn

Batteries & Supercaps

Research Article
doi.org/10.1002/batt.202400426

Chemistry
Europe

European Chemical
Societies Publishing

electrode also shows good cycling stability after 5000 cycles with a coulombic efficiency of ~100%. Furthermore, an ammonium-ion full cell of VO-EDA//NiHCF exhibits a specific capacity of 55 mAh g^{-1} at 0.1 A g^{-1} and excellent long-term cycling stability with 89.5% capacity retention after 10000 cycles at 5 A g^{-1}.

Results and Discussion

The synthesis procedure of VO-EDA and VO–N is illustrated in Figure 1a. Briefly, VO-EDA was synthesized via a one-step solvothermal method starting with NH$_4$VO$_3$ and 1,2-ethylenediamine (EDA) with a certain pH value. The VO–N sample was prepared using a similar method without the addition of EDA. The crystal structures of the as-prepared samples were characterized by the X-ray diffraction (XRD), as shown in Figure 1b. All the peaks of the VO-EDA can be assigned to the V$_3$O$_7 \cdot$H$_2$O phase (JCPDA No. 28–1433), and the peak located at 10.4° is shifted to the lower degree of 10.0°, suggesting that EDA may intercalate into the interlayer of vanadium oxide compounds.

As for VO–N sample, the diffraction signals fit well with the standard data of (NH$_4$)$_2$V$_6$O$_{16}$ (JCPDS No. 22–1046). This result suggests that the introduction of EDA can effectively control the phase of samples. Scanning electron microscope (SEM) images show that the VO-EDA is composed of ultrathin nanorod (Figure 1d), while the VO–N consists of unevenly sized nanosheets (Figure 1c). The selected area electron diffraction (SAED) pattern (Figure 1e) of the VO-EDA presents the corresponding diffraction spot at the (121) and (321) planes, further indicating the crystallized characteristics of our prepared VO-EDA. Besides, the high-resolution TEM (HRTEM) of VO-EDA sample in Figure S1(a) displayed that the lattice distance of 0.199 nm is corresponded to (071) phase of V$_3$O$_7 \cdot$H$_2$O (JCPDA No. 28–1433). An interlayer distance of 0.174 nm was measured for VO–N (Figure S1(b)), which is well indexed to the (401) plane of (NH$_4$)$_2$V$_6$O$_{16}$ (JCPDS No. 22–1046). Additionally, the energy dispersive spectroscopy (EDS) elemental mapping images clearly show the homogeneously distribution of O, V, N and C elements on nanorods (Figure 1f).

To further investigate the composition of VO-EDA and VO–N samples, quantitative analysis was characterized by
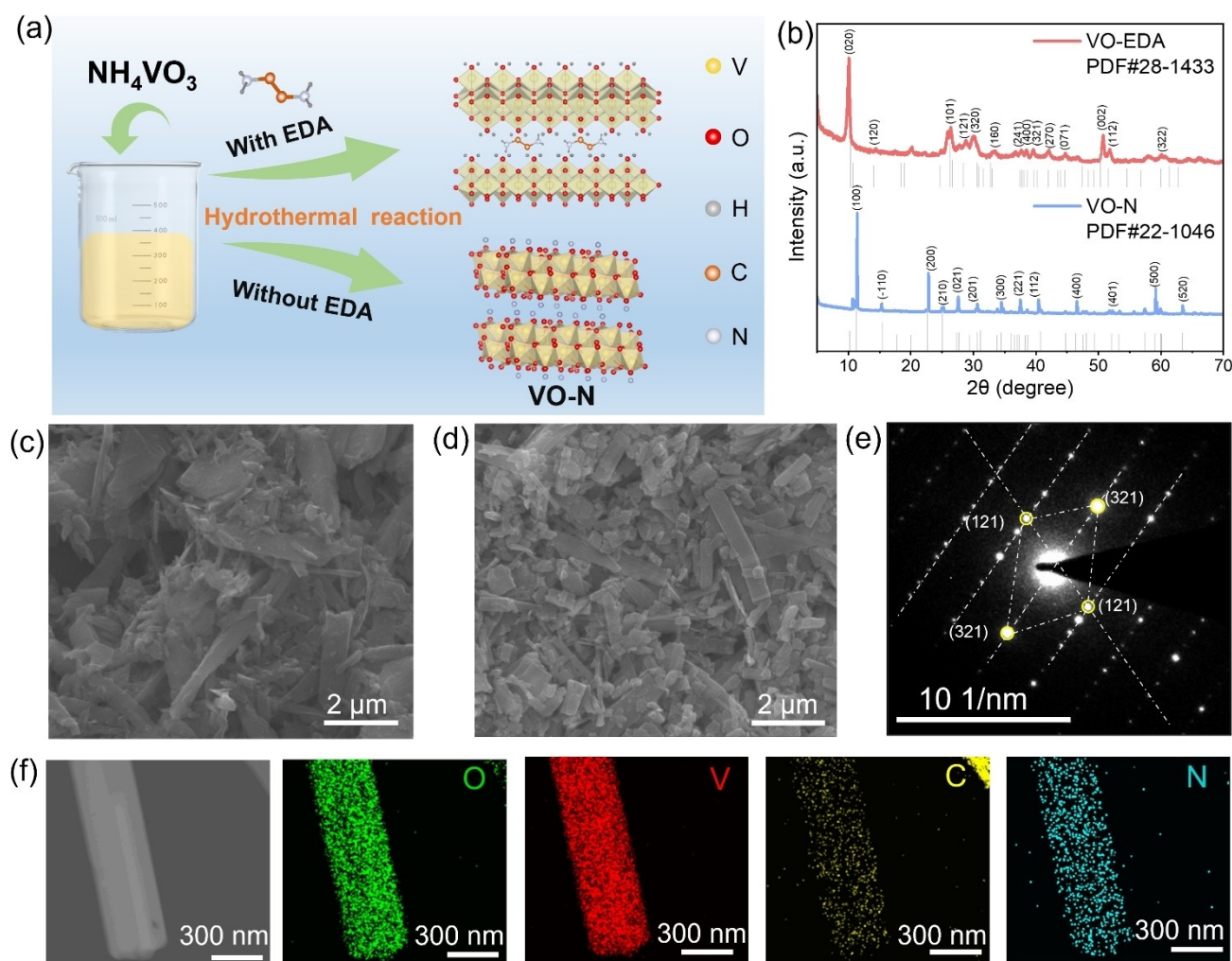

Figure 1. (a) Schematic illustration of the synthesis process of VO-EDA and VO–N. (b) XRD patterns of VO-EDA and VO–N samples. SEM images of (c) VO–N and (d) VO-EDA. (e) SAED pattern and (f) the EDS elemental mapping images of VO-EDA sample.

thermogravimetric analysis (TGA). As shown in Figure 2a, TGA curve of VO-EDA undergoes two stages of weight loss. The first stage is the loss of lattice water molecules, and the second stage is ascribed to the removal of EDA molecules.[29] In comparison, the VO–N only experiences a decomposition process. The chemical composition of VO-EDA was further confirmed by elemental analyzer. The weight percentage are 4.05 for C, 2.03 for H and 4.30 for N, suggesting that VO-EDA is $V_3O_7 \cdot 1.12H_2O \cdot (C_{1.06}N_{0.98}H_{4.12})$.[30] From the Raman spectrum (Figure S2), the VO-EDA samples showed a peak at 138 cm^{-1} associated with the layered structure.[31] In the Fourier transform infrared (FT-IR) spectra (Figure 2b), the peaks at about 529 and 927 cm^{-1} corresponding to the V–O and V=O bonds are observed in the VO-EDA and VO–N samples.[32,33] Notably, the C–N, C–H and C–N vibration are detected in the VO-EDA sample, which were located at 1329 cm^{-1}, 1497 cm^{-1} and 1599 cm^{-1}, respectively, further confirming the presence of EDA.[29] More importantly, the peak at 3007 cm^{-1} further suggests the successful formation of hydrogen bond between EDA and the oxygen atom of vanadium oxide.[21] X-ray photoelectron spectroscopy (XPS) characterizations were conducted to further investigate the detailed chemical composition and valence state of the obtained samples. In the high-resolution XPS spectra of V 2p (Figure 2c), two peaks located at 524.7 and 517.2 eV were attributed to the V $2p_{1/2}$ and V $2p_{3/2}$ of V^{5+}, respectively, while the peaks of V $2p_{3/2}$ and V $2p_{1/2}$ located at 523.4 and 517.9 eV can be ascribed to the V^{4+}.[34] Compared with VO–N, VO-EDA has a much higher V^{4+} content, which is accompanied by a higher generation of oxygen defects (Figure 2d). In the spectrum of O 1s, the peaks located at 532.5 eV corresponding to H$_2$O further confirm the water molecules in

the interlayer of VO-EDA.[35] The N 1s spectra of VO–N can be deconvoluted into two N containing components for NH$_4^+$, i.e., –NH$^+$– (401.8 eV) and –NH– (401.1 eV). In the N 1s spectra of VO-EDA, two peaks located at 400.0 eV and 401.6 eV correspond to the –C–NH$_2$– and –NH–, further suggesting that the successful insertion of EDA (Figure 2e).[36] As shown in Figures S3 and S4, VO-EDA and VO–N own similar surface area and wettability to the electrolyte. The successful introduction of EDA into the interlayer of VO-EDA can improve its conductivity, which is evidenced by the electrochemical impedance spectroscopy (EIS) measurements. As shown in Figure 2f, the diameter of the semicircle (related to interface charge transfer resistance (Rct)) for VO-EDA (7.5 Ω) is smaller than that of VO–N (10.6 Ω), suggesting that the intercalation of the EDA can promote the charge transport by reducing the interface charge transfer resistance.

The electrochemical performance of VO-EDA was first studied by cyclic voltammetry (CV) in a three-electrode configuration with a saturated calomel electrode as reference electrode, carbon rod as counter electrode and 1 M NH$_4$Ac as electrolyte. The redox peaks with no significantly change can be observed for the VO-EDA electrode in the first five cycles, which indicates that the electrochemical reaction is highly reversible (Figure S5). Figure 3a compares the CV curves of VO-EDA and VO–N electrodes. The redox peaks at around −0.03 V and −0.43 V correspond to the reduction of V,[37] and the successive intercalation of NH$_4^+$ ions.[38] In contrast to the VO–N electrode, VO-EDA electrode displays higher current density, suggesting the improved reaction activity. The GCD profiles of VO-EDA and VO–N electrodes at 1 A g^{-1} are shown in Figure 3b, which demonstrates one charge and discharge platform consistent
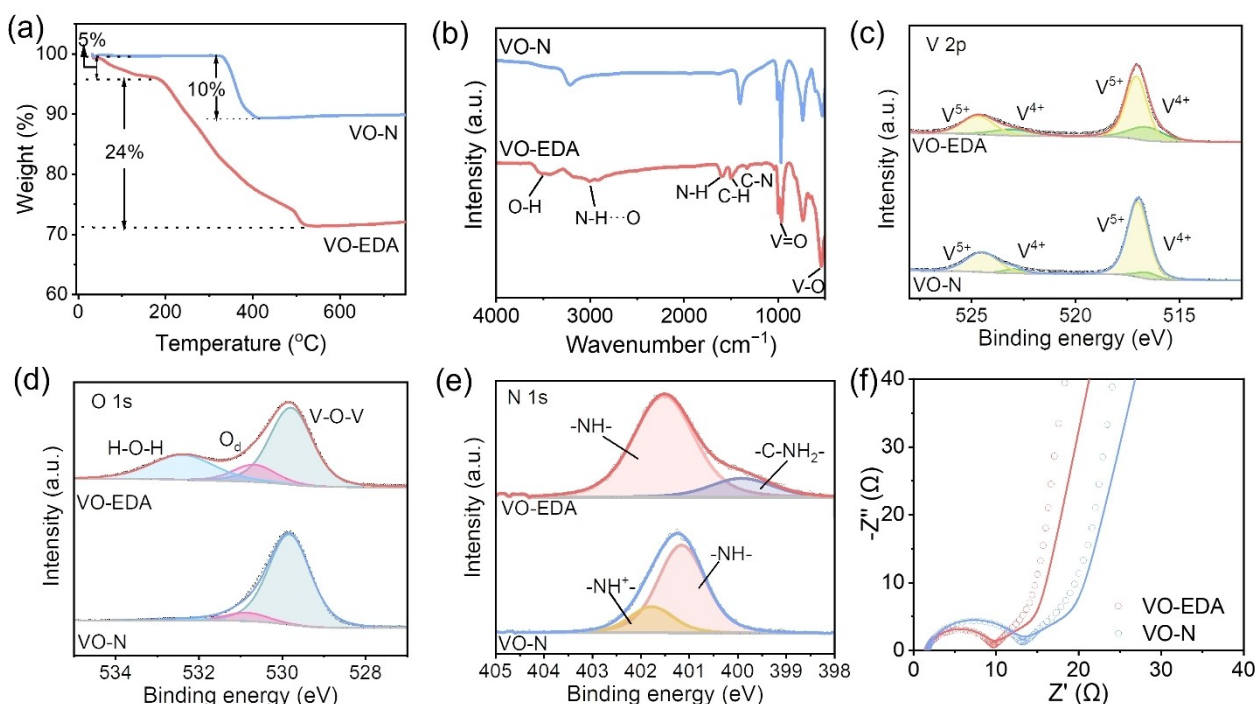

Figure 2. (a) TG curves and (b) FT-IR spectra of VO-EDA and VO–N samples. (c) V 2p, (d) O 1s and (e) N 1s XPS spectra of VO-EDA and VO–N samples. (f) EIS measurements of VO-EDA and VO–N samples.
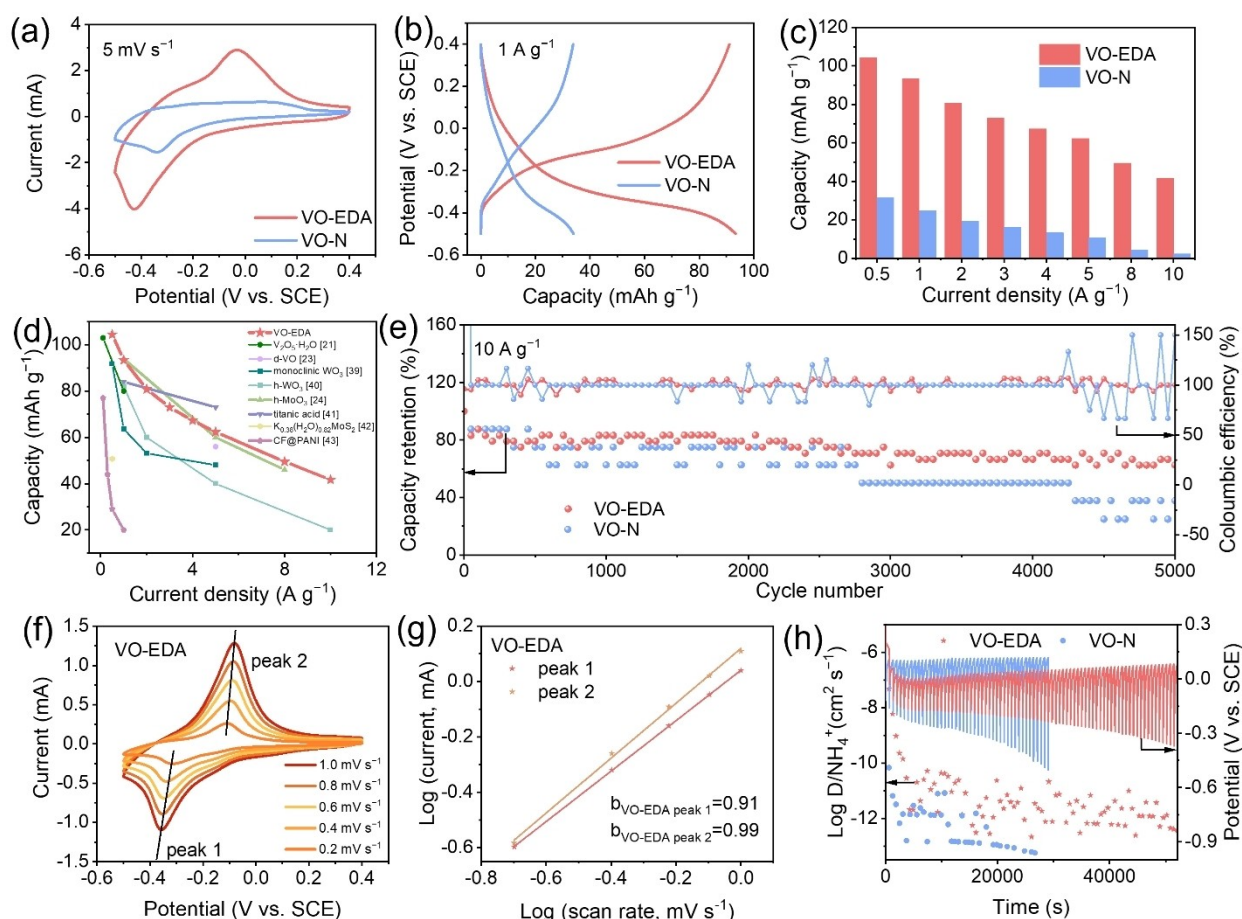
Batteries & Supercaps

Research Article
doi.org/10.1002/batt.202400426

Chemistry
Europe

European Chemical
Societies Publishing

Figure 3. (a) CV curves at 5 mV s^{-1}, (b) GCD curves at 1 A g^{-1} and (c) capacity comparison at different current densities of VO-EDA and VO–N electrodes. (d) Capacity comparison of VO-EDA electrode with state-of-the-art NH_4^+ storage materials. (e) Cycling stability of VO-EDA and VO–N at 10 A g^{-1}. (f) CV curves from 0.2 mV s^{-1} to 1.0 mV s^{-1} and (g) log (current) versus log (scan rate) plots of five redox peaks in CV curves of VO-EDA electrode. (h) GITT curves of VO-EDA and VO–N electrodes.

with the CV tests. Impressively, the VO-EDA electrode exhibits a specific capacity of 93.4 mAh g^{-1}, far surpassing that of VO–N electrode (24.7 mAh g^{-1}) at current density of 1 A g^{-1}. To further demonstrate the superior NH4$^+$ storage capability of VO-EDA electrode, the specific capacity obtained at different current densities from 0.5 A g^{-1} to 10 A g^{-1} are compared in Figure 2c. At the low current density of 0.5 A g^{-1}, the VO-EDA electrode delivers 104.4 mAh g^{-1}. Increasing the current density to 10.0 A g^{-1}, the capacity of VO-EDA electrode remains at 41.7 mAh g^{-1}, demonstrating its excellent rate performance. In contrast, the specific capacity of VO–N electrode is significantly lower, dropping rapidly to 2.4 mAh g^{-1} especially at high current density of 10 A g^{-1}. Additionally, we also explored the effect of the amount of EDA on electrode performance. Evidently, the amount of EDA did not significantly affect the crystal structure of vanadium oxides (Figure S6), in which the VO-EDA exhibited the highest crystalline. The GCD curves and stability test in Figure S7 showed that the capacity and cycling stability of the VO-EDA electrodes are superior to those of the VO-05EDA and VO-2EDA electrodes. Furthermore, the specific capacity of VO-EDA electrode is considerable or better than those of recently reported ammonium ion storage materials,

such as V$_2$O$_5$·H$_2$O,[21] d-VO,[23] monoclinic WO$_3$,[39] h-WO$_3$,[40] h-MoO$_3$[24] titanic acid,[41] K$_{0.38}$(H$_2$O)$_{0.82}$MoS$_2$[42] and CF@PANI[43] (Figure 3d). Figure 3e and Table S1 displays the long cycle life of the VO-EDA and VO–N electrodes at 10 A g^{-1}. The capacity retention of VO-EDA electrodes after 5000 cycles is as high as 66.6%, which is significantly better than that of VO–N electrodes (37.8%). The corresponding average coulombic efficiency of the VO-EDA electrode is ~100% while the coulombic efficiency of VO–N is fluctant, which can be ascribed to the side reaction.[44] This demonstrate the highly reversibility of the NH$_4^+$ embedding and stripping reactions.

To further understand the electrochemical reaction kinetics of VO-EDA electrode, the CV tests under different scan rates from 0.2 mV s^{-1} to 1 mV s^{-1} was collected at −0.5–0.4 V. As shown in Figure 3f, all the CV curves exhibit similar shapes, and the polarization induces an increase in the cathodic peak position and a decrease in the anodic peak with increasing scan rates. The peak current (i) and the scan rate (v) have been reported to obey the following equation:

$$i = av^b \tag{1}$$

Batteries & Supercaps

Research Article
doi.org/10.1002/batt.202400426

Chemistry Europe
European Chemical
Societies Publishing

$$logi = blogv + loga \qquad (2)$$

where a and b are variable parameters. Specifically, the value of b closing to 1 represent the capacitive-controlled process, while the b value of 0.5 corresponds to the diffusion-limited process.[45] Figure 3g displays the fitted plots, in which the b values of peaks 1 and 2 are 0.91 and 0.99. This fitting results demonstrate that the NH_4^+ storage of VO-EDA is mainly dominated by capacitive-controlled mechanism. Similarly, the same mechanism was obtained for the NH_4^+ storage of VO–N (Figure S8). It should be noted that VO-EDA exhibits a higher electrochemical active area than VO–N (Figure S9), which favors NH_4^+ storage. To further probe the enhanced NH_4^+ storage performance, the diffusion coefficient of NH_4^+ ($D_{NH_4^+}$) in VO-EDA was estimated by galvanostatic intermittent titration technique (GITT) (Figure 3h). The average $D_{NH_4^+}$ value of VO-EDA at the discharge was 6.8×10^{-10} $cm^2\,S^{-1}$, much higher than that of

VO–N (3.2×10^{-12} $cm^2\,S^{-1}$), indicating fast mobility during NH_4^+ storage.

The NH_4^+ storage mechanism of VO-EDA is further evaluated via the ex-situ SEM, XRD and XPS. Figure 4a gives the typical charge/discharge curve of the VO-EDA for the first cycle, along with the labeled states (points A–E). Evidently, the morphologies of VO-EDA did not change significantly during the charge/discharge process (Figure 4b), indicating its good morphological reversibility. Figure 4c presents the ex-situ XRD patterns of VO-EDA at different charge/discharge states. At the initial state (state A), the peak of (020) plane was located at 10.2° and shifted to a high angle when discharging to −0.3 V and −0.5 V (state B and C), demonstrating the that intercalated NH_4^+ with the formation of hydrogen bonding reduces the interlayer distance.[46] Upon charging from state C (−0.5 V) to E (0.4 V), the (020) peak deviated to lower angles and recovered to the initial position, suggesting the deintercalation of NH_4^+. These suggest that VO-EDA owns good structural reversibility during the electrochemical reaction. Figure 4d and e shows the
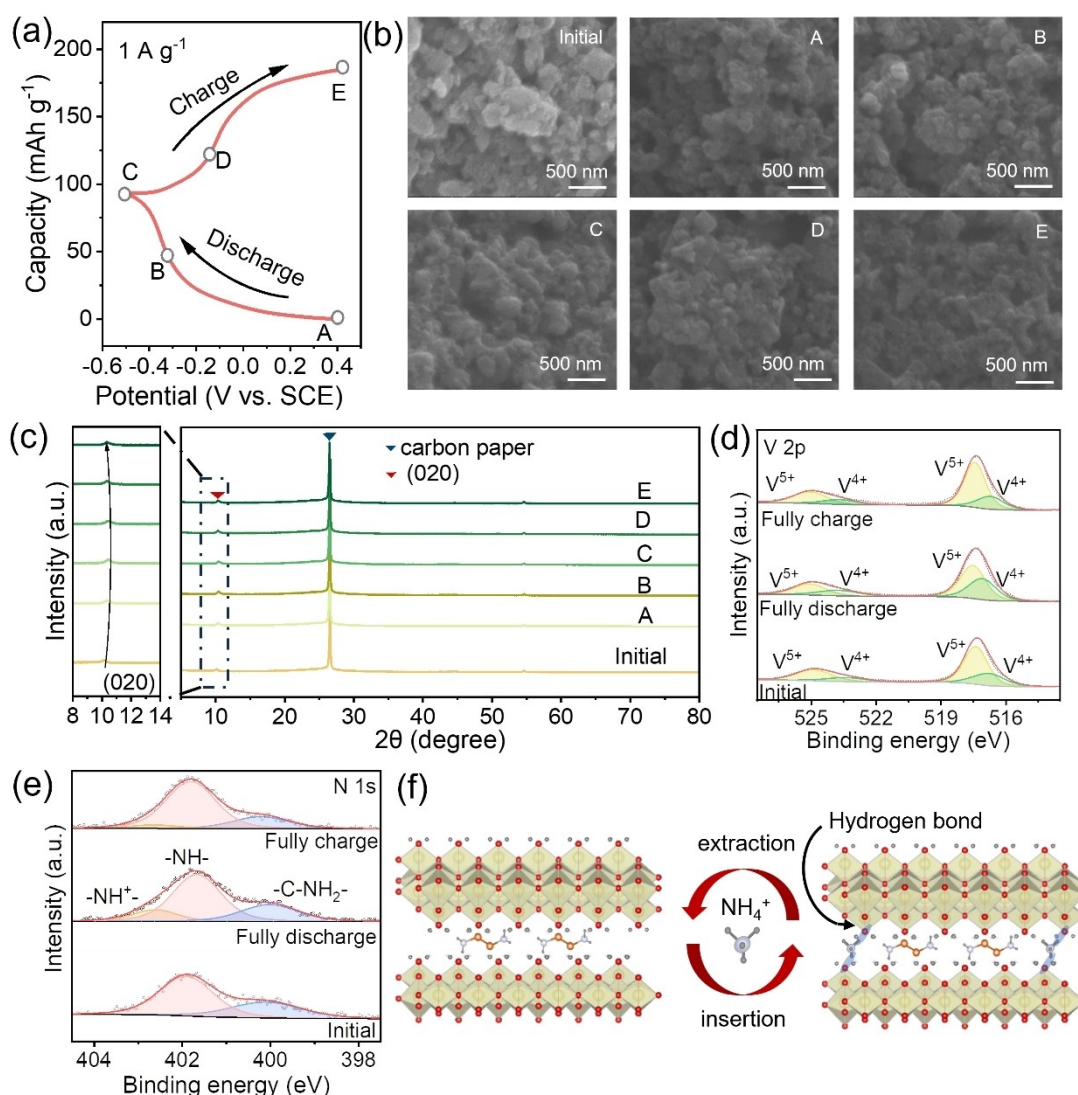

Figure 4. (a) GCD curves of VO-EDA at 1 A g^{-1}, (b) SEM images, (c) XRD patterns, (c) V 2p XPS spectra, and (e) N 1s XPS spectra of VO-EDA electrode at specific potential states. (f) Schematic illustration of the NH_4^+ mechanism and storage in VO-EDA.

Batteries & Supercaps

Research Article
doi.org/10.1002/batt.202400426

Chemistry Europe
European Chemical
Societies Publishing

V 2p and N 1s XPS spectra of VO-EDA electrode at different discharging/charging states. Compared to the initial states of VO-EDA, the V^{4+} has a significant increase during discharge to −0.5 V while the ratio of V^{5+} decrease, suggesting that the intercalation of NH_4^+ can result in the reduction of V^{5+} to V^{4+}. On the contrary, after fully charging to 0.4 V, the increase of V^{5+} and the decrease of V^{4+} attribute to the de-intercalation of NH_4^+ gives the rise to the oxidation of V^{4+} to V^{5+} (Figure 4d).[27] The N 1s XPS spectra of the fully discharged electrode can be deconvoluted into three different peaks, located at 402.6 eV (−NH^+−), 401.6 eV (−NH−) and 400.0 eV (−C−NH_2−). The ratio of −NH^+−/−C−NH_2− (53.1%) increases compared to those at initial (0%) and charge states (26.1%), suggesting the successful intercalation of the ammonium ion.[34] The NH_4^+ storage mechanism of VO-EDA is schematically illustrated in Figure 4f.

To verify the feasibility of VO-EDA anode, an aqueous ammonium-ion full cell was assembled using a Prussian analogue NiHCF as the cathode, and 1.0 M NH_4Ac as the electrolyte (Figure 5a) (denoted as VO-EDA//NiHCF). The NiHCF was synthesized by a simple co-deposition method (see Experimental section for detailed synthesis).[47] The SEM images in Figure S10 show that NiHCF comprises two-dimensional nanosheets. XRD pattern also confirms that the as-prepared NiHCF is a highly pure product which can be indexed to NONiFe(CN)$_5$ (JCPDS No. 23–0426) (Figure S11). The CV and GCD results of NiHCF demonstrate that it is well suited as a cathode for ammonium ion full cell (Figure S12). The first five CV curves of VO-EDA//NiHCF at 5 mVs^{-1} are shown in Figure 5b, where one pair redox peaks are observed which are located at 0.5 V and 0.8 V. Also, the highly overlapping CV curves demonstrate that the VO-EDA//NiHCF is highly reversible. Figure 5c shows the galvanostatic charge/discharge profiles of VO-EDA//NiHCF from 0.1 to 5 Ag^{-1}. A high specific capacity of 60 mAhg^{-1} at 0.1 Ag^{-1} was obtained. The rate capability of VO-EDA//NiHCF is further explored at different current densities (Figure 3d). Specifically, the initial capacity of VO-EDA//NiHCF is 55 mAhg^{-1} at a low current density of 0.1 Ag^{-1}. When the current density increases to 5 Ag^{-1}, an average capacity of 22 mAhg^{-1} is still retained. Meanwhile, the specific capacity of VO-EDA//NiHCF can be restored to 61 mAhg^{-1} when the current density is reduced back to 0.1 Ag^{-1} after 80 cycles. In contrast, VO-N//NiHCF exhibits a lower specific capacity at different current densities (Figure S13). In addition, VO-EDA//NiHCF also present excellent cycling stability compared to VO-N//NiHCF. As shown in Figure 5e, VO-EDA//NiHCF displays a capacity retention of 88.6% after 10000 cycles at 5 Ag^{-1}, significantly better than that of VO-N//NiHCF (54.2%). Impressively, the average coulombic efficiency of VO-EDA//NiHCF was
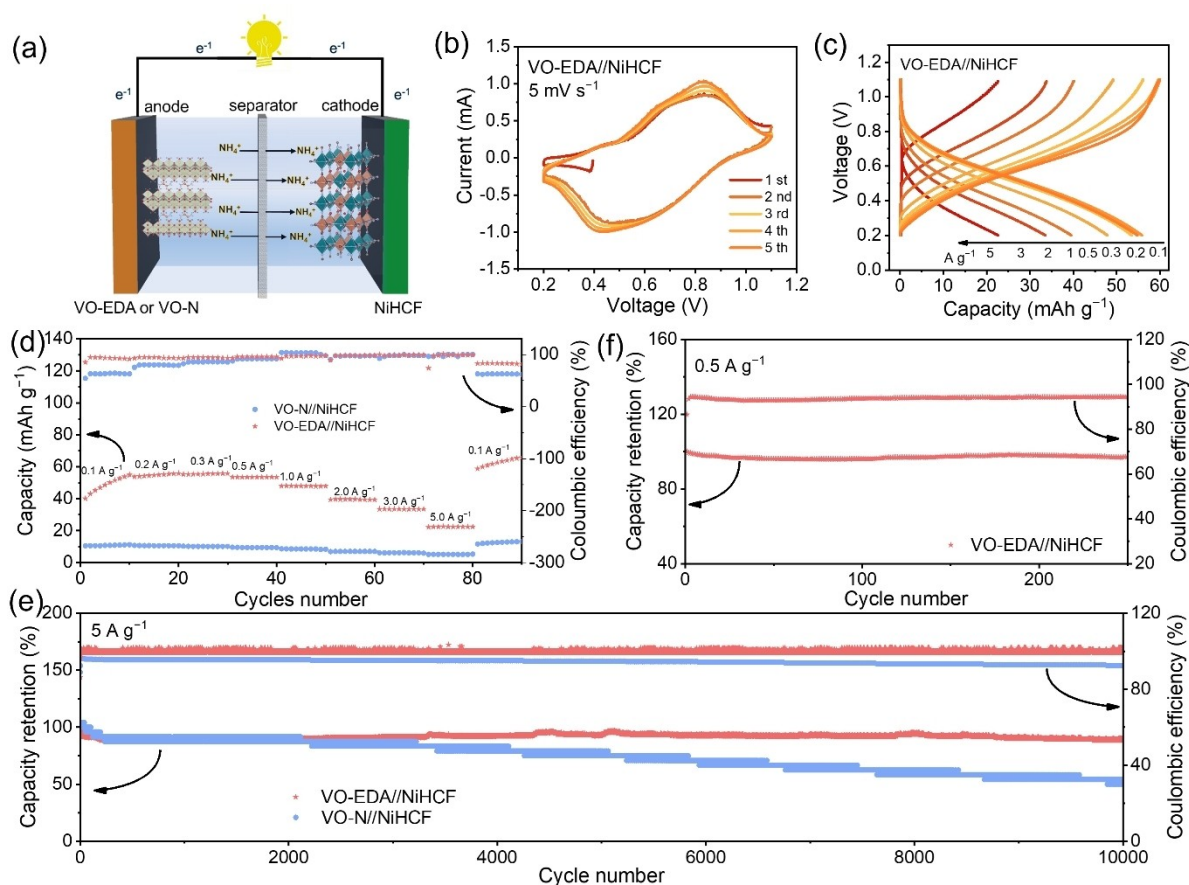

Figure 5. (a) Schematic illustration of the aqueous ammonium-ion full cell. (b) First five CV curves at 5 mVs^{-1} and (c) GCD curves at different current densities of VO-EDA//NiHCF. (d) Rate performance of VO-EDA//NiHCF and VO–N//NiHCF. (e) Cycling stability of VO-EDA//NiHCF and VO–N//NiHCF at 5 Ag^{-1}. (f) Cycling performance of VO-EDA//NiHCF at 0.5 Ag^{-1}.

maintained at 99.9% during the cycling processes. Furthermore, VO-EDA//NiHCF also exhibits a considerable capacity retention of 97.2% after 250 cycles even at the low current density of 0.5 A g^{-1} (Figure 5f and Table S2). The above results demonstrate that ethanediamine could serve as pillars in the interlayer of VO-EDA to enable better cycling stability than ammonium ions intercalated VO−N.

Conclusions

In conclusion, we prepared an organic-inorganic hybrid material of VO-EDA by a one-step solvothermal method and used it as an anode for AAIBs. The intercalated EDA molecules could bind to NH$_4^+$ as an electron donor, providing more sites to store NH$_4^+$. Moreover, the hydrogen bonding network between EDA and vanadium oxides could facilitate charge transfer. The as-synthesized VO-EDA electrode displays a high capacity of 104.4 mAh g^{-1} at 0.5 A g^{-1} and considerable cycling stability with the capacity retention of 62.5% after 5000 cycles at 10 A g^{-1}, outperforming the intrinsic VO−N (24.7 mAh g^{-1}, 37.8% after 5000 cycles). In addition, the highly reversible NH$_4^+$ (de)intercalation into the layered VO-EDA crystal structure was systematically characterized by SEM, XRD and XPS analyses. Furthermore, the VO-EDA//NiHCF AAIBs delivers an excellent cycling stability with only 11.4% capacity decline after 10000 cycles at 5 A g^{-1}, showing potential applications.

Supporting Information Summary

Supplementary data associated with this article can be found in the online version.

Acknowledgements

Conflict of Interests

The authors declare no conflict of interest.

Data Availability Statement

The data that support the findings of this study are available in the supplementary material of this article.

[1] Z. Wang, Y. Li, J. Wang, R. Ji, H. Yuan, Y. Wang, H. Wang, *Carbon Energy* **2022**, *4*, 411–445.
[2] X. Gao, H. Zhang, X. Liu, X. Lu, *Carbon Energy* **2020**, *2*, 387–407.
[3] S. Liu, G. Pan, G. Li, X. Gao, *J. Mater. Chem. A* **2015**, *3*, 959–962.
[4] Y. Zeng, Z. Lai, Y. Han, H. Zhang, S. Xie, X. Lu, *Adv. Mater.* **2018**, *30*, 1802396.
[5] W. Liang, Y. Che, Z. Cai, R. Tang, Z. Ma, X. Zheng, X. Wu, J. Li, H. Jin, C. Zhu, T. Chen, *Adv. Funct. Mater.* **2023**, *34*, 2304798.
[6] S. Wang, H. Zhang, K. Zhao, W. Liu, N. Luo, J. Zhao, S. Wu, J. Ding, S. Fang, F. Cheng, *Carbon Energy* **2023**, *5*, e330.
[7] F. Wang, X. Fan, T. Gao, W. Sun, Z. Ma, C. Yang, F. Han, K. Xu, C. Wang, *ACS Cent. Sci.* **2017**, *3*, 1121–1128.
[8] R. Cang, C. Zhao, K. Ye, J. Yin, K. Zhu, J. Yan, G. Wang, D. Cao, *ChemSusChem* **2020**, *13*, 3911–3918.
[9] C. Yang, J. Chen, X. Ji, T. P. Pollard, X. Lü, C. Sun, S. Hou, Q. Liu, C. Liu, T. Qing, Y. Wang, O. Borodin, Y. Ren, K. Xu, C. Wang, *Nature* **2019**, *569*, 245–250.
[10] Z. Li, D. Young, K. Xiang, W. C. Carter, Y. Chiang, *Adv. Energy Mater.* **2012**, *3*, 290–294.
[11] L. Suo, O. Borodin, Y. Wang, X. Rong, W. Sun, X. Fan, S. Xu, M. A. Schroeder, A. V. Cresce, F. Wang, C. Yang, Y. S. Hu, K. Xu, C. Wang, *Adv. Energy Mater.* **2017**, *7*, 1701189.
[12] D. Su, A. McDonagh, S. Qiao, G. Wang, *Adv. Mater.* **2016**, *29*, 1604007.
[13] J. Buffle, Z. Zhang, K. Startchev, *Environ. Sci. Technol.* **2007**, *41*, 7609–7620.
[14] R. Zhang, S. Wang, S. Chou, H. Jin, *Adv. Funct. Mater.* **2022**, *32*, 2112179.
[15] M. Xia, X. Zhang, H. Yu, Z. Yang, S. Chen, L. Zhang, M. Shui, Y. Xie, J. Shu, *Chem. Eng. J.* **2021**, *421*, 127759.
[16] X. Wu, Y. Qi, J. J. Hong, Z. Li, A. S. Hernandez, X. Ji, *Angew. Chem. Int. Ed.* **2017**, *56*, 13026–13030.
[17] C. Li, W. Yan, S. Liang, P. Wang, J. Wang, L. Fu, Y. Zhu, Y. Chen, Y. Wu, W. Huang, *Nanoscale Horiz.* **2019**, *4*, 991–998.
[18] L. Yan, Y. Qi, X. Dong, Y. Wang, Y. Xia, *eScience* **2021**, *1*, 212–218.
[19] Y. Song, Q. Pan, H. Lv, D. Yang, Z. Qin, M. Zhang, X. Sun, X. Liu, *Angew. Chem. Int. Ed.* **2021**, *60*, 5718–5722.
[20] D. Yang, Y. Song, M. Zhang, Z. Qin, J. Liu, X. Liu, *Angew. Chem. Int. Ed.* **2022**, *61*, e202207711.
[21] S. Dong, W. Shin, H. Jiang, X. Wu, Z. Li, J. Holoubek, W. F. Stickle, B. Key, C. Liu, J. Lu, P. A. Greaney, X. Zhang, X. Ji, *Chem* **2019**, *5*, 1537–1551.
[22] X. Zhang, H. Wei, B. Ren, J. Jiang, G. Qu, J. Yang, G. Chen, H. Li, C. Zhi, Z. Liu, *Adv. Mater.* **2023**, *35*, 2304209.
[23] Y. Wu, S. Dong, N. Lv, Z. Xu, R. Ren, G. Zhu, B. Huang, Y. Zhang, X. Dong, *Small* **2022**, *18*, 2204888.
[24] G. Liang, Y. Wang, Z. Huang, F. Mo, X. Li, Q. Yang, D. Wang, H. Li, S. Chen, C. Zhi, *Adv. Mater.* **2020**, *32*, e1907802.
[25] Y. Lin, L. Ta, J. Meng, Y. Song, X. Liu, *Chem. Commun.* **2023**, *59*, 1481–1484.
[26] W. Liang, D. Rao, T. Chen, R. Tang, J. Li, H. Jin, *Angew. Chem. Int. Ed.* **2022**, *61*, e202207779.
[27] S. F. Kuchena, Y. Wang, *Electrochim. Acta* **2022**, *425*, 140751.
[28] X. Bai, J. Yang, F. Zhang, Z. Jiang, F. Sun, C. Pan, H. Di, S. Ru, D. Liao, H. Zhang, *Dalton Trans* **2023**, *52*, 4923–4932.
[29] X. Ma, X. Cao, M. Yao, L. Shan, X. Shi, G. Fang, A. Pan, B. Lu, J. Zhou, S. Liang, *Adv. Mater.* **2021**, *34*, 2105452.
[30] M. Roppolo, C. B. Jacobs, S. Upreti, N. A. Chernova, M. S. Whittingham, *J. Mater. Sci.* **2008**, *43*, 4742–4748.
[31] T. Selvam, N. T. Bharanitharan, D. Dhinasekaran, B. Subramanian, A. R. Rajendran, *ACS Appl. Energy Mater.* **2023**, *7*, 93–103.
[32] P. Han, H. Wang, Z. Liu, X. Chen, W. Ma, J. Yao, Y. Zhu, G. Cui, *Carbon* **2011**, *49*, 693–700.
[33] K. Wang, F. Liu, Q. Li, J. Zhu, X. Qiu, X. Liu, X. Sun, *Chem. Eng. J.* **2023**, *452*, 139577.
[34] D. Yu, Z. Wei, X. Zhang, Y. Zeng, C. Wang, G. Chen, Z. X. Shen, F. Du, *Adv. Funct. Mater.* **2020**, *31*, 2008743.
[35] X. Cheng, Z. Xiang, C. Yang, Y. Li, L. Wang, Q. Zhang, *Adv. Funct. Mater.* **2023**, *34*, 2311412.
[36] J. Meng, Z. Lan, T. Chen, Q. Lin, H. Liu, X. Wei, Y. Lu, J. Li, Z. Zhang, *J. Phys. Chem. C* **2018**, *122*, 24725–24731.

Batteries & Supercaps

Research Article
doi.org/10.1002/batt.202400426

Chemistry Europe
European Chemical
Societies Publishing

[37] L. Xing, H. Chen, X. Wen, W. Zhou, K. Xiang, *J. Alloys Compd.* **2022**, *925*, 166652.

[38] C. Han, J. Zhu, K. Fu, D. Deng, W. Luo, L. Mai, *Chem. Commun.* **2022**, *58*, 791–794.

[39] X. Wen, J. Luo, K. Xiang, W. Zhou, C. Zhang, H. Chen, *Chem. Eng. J.* **2023**, *458*, 141381.

[40] Y. Z. Zhang, J. Liang, Z. Huang, Q. Wang, G. Zhu, S. Dong, H. Liang, X. Dong, *Adv. Sci.* **2022**, *9*, e2105158.

[41] J. Holoubek, H. Jiang, D. Leonard, Y. Qi, G. Bustamante, X. Ji, *Chem. Commun.* **2018**, *54*, 9805–9808.

[42] M. Xie, W. Zhao, Y. Mao, F. Huang, *Dalton Trans.* **2020**, *49*, 3488–3494.

[43] H. Li, J. Yang, J. Cheng, T. He, B. Wang, *Nano Energy* **2020**, *68*, 104369.

[44] H. Chen, X. Zhang, S. Zhang, S. Wu, F. Chen, J. Xu, *Chem. Eng. J.* **2022**, *429*, 132403.

[45] L. Dua, S. Bi, M. Yanga, Z. Tie, M. Zhanga, Z. Niua, *Proc. Natl. Acad. Sci.* **2022**, *119*, e2214545119.

[46] F. Ye, R. Pang, C. Lu, Q. Liu, Y. Wu, R. Ma, L. Hu, *Angew. Chem. Int. Ed.* **2023**, *62*, e202303480.

[47] Y. Gao, H. Yang, X. Wang, Y. Bai, N. Zhu, S. Guo, L. Suo, H. Li, H. Xu, C. Wu, *ChemSusChem* **2020**, *13*, 732–740.